Astronomy & Astrophysics manuscript no. ajbohn_yses_companion_tyc8984
April 22, 2021

Discovery of a directly imaged planet to the young solar analog YSES 2⋆

Alexander J. Bohn[1], Christian Ginski[2,1], Matthew A. Kenworthy[1], Eric E. Mamajek[3,4], Mark J. Pecaut[5], Markus Mugrauer[6], Nikolaus Vogt[7], Christian Adam[7,8], Tiffany Meshkat[9], Maddalena Reggiani[10], and Frans Snik[1]

[1] Leiden Observatory, Leiden University, PO Box 9513, 2300 RA Leiden, The Netherlands
e-mail: bohn@strw.leidenuniv.nl
[2] Sterrenkundig Instituut Anton Pannekoek, Science Park 904, 1098 XH Amsterdam, The Netherlands
[3] Jet Propulsion Laboratory, California Institute of Technology, 4800 Oak Grove Drive, M/S 321-100, Pasadena CA 91109, USA
[4] Department of Physics & Astronomy, University of Rochester, Rochester NY 14627, USA
[5] Rockhurst University, Department of Physics, 1100 Rockhurst Road, Kansas City MO 64110, USA
[6] Astrophysikalisches Institut und Universitäts-Sternwarte Jena, Schillergäßchen 2, D-07745 Jena, Germany
[7] Instituto de Física y Astronomía, Facultad de Ciencias, Universidad de Valparaíso, Av. Gran Bretaña 1111, Playa Ancha, Valparaíso, Chile
[8] Núcleo Milenio Formación Planetaria - NPF, Universidad de Valparaíso, Av. Gran Bretaña 1111, Valparaíso, Chile
[9] IPAC, California Institute of Technology, M/C 100-22, 1200 East California Boulevard, Pasadena CA 91125, USA
[10] Institute of Astronomy, KU Leuven, Celestijnenlaan 200D, B-3001 Leuven, Belgium

Received February 6, 2021 / Accepted <date>

ABSTRACT

Context. To understand the origin and formation pathway of wide-orbit gas giant planets, it is necessary to expand the limited sample of these objects. The mass of exoplanets derived with spectrophotometry, however, varies strongly as a function of the age of the system and the mass of the primary star.

Aims. By selecting stars with similar ages and masses, the Young Suns Exoplanet Survey (YSES) aims to detect and characterize planetary-mass companions to solar-type host stars in the Scorpius-Centaurus association.

Methods. Our survey is carried out with VLT/SPHERE with short exposure sequences on the order of 5 min per star per filter. The subtraction of the stellar point spread function (PSF) is based on reference star differential imaging (RDI) using the other targets (with similar colors and magnitudes) in the survey in combination with principal component analysis. Two astrometric epochs that are separated by more than one year are used to confirm co-moving companions by proper motion analysis.

Results. We report the discovery of YSES 2b, a co-moving, planetary-mass companion to the K1 star YSES 2 (TYC 8984-2245-1, 2MASS J11275535-6626046). The primary has a Gaia EDR3 distance of 110 pc, and we derive a revised mass of 1.1 $M_\odot$ and an age of approximately 14 Myr. We detect the companion in two observing epochs southwest of the star at a position angle of 205° and with a separation of $\sim 1\farcs05$, which translates to a minimum physical separation of 115 au at the distance of the system. Photometric measurements in the H and K_s bands are indicative of a late L spectral type, similar to the innermost planets around HR 8799. We derive a photometric planet mass of $6.3^{+1.6}_{-0.9}\,M_\mathrm{Jup}$ using AMES-COND and AMES-dusty evolutionary models; this mass corresponds to a mass ratio of $q = (0.5 \pm 0.1)\,\%$ with the primary. This is the lowest mass ratio of a direct imaging planet around a solar-type star to date. We discuss potential formation mechanisms and find that the current position of the planet is compatible with formation by disk gravitational instability, but its mass is lower than expected from numerical simulations. Formation via core accretion must have occurred closer to the star, yet we do not find evidence that supports the required outward migration, such as via scattering off another undiscovered companion in the system. We can exclude additional companions with masses greater than 13 M_Jup in the full field of view of the detector ($0\farcs15 < \rho < 5\farcs50$), at $0\farcs5$ we can rule out further objects that are more massive than 6 M_Jup, and for projected separations $\rho > 2''$ we are sensitive to planets with masses as low as 2 M_Jup.

Conclusions. YSES 2b is an ideal target for follow-up observations to further the understanding of the physical and chemical formation mechanisms of wide-orbit Jovian planets. The YSES strategy of short snapshot observations ($\leq$ 5 min) and PSF subtraction based on a large reference library proves to be extremely efficient and should be considered for future direct imaging surveys.

Key words. Planets and satellites: detection — Planets and satellites: formation — Instrumentation: high angular resolution — Techniques: image processing — Stars: individual: YSES 2 (TYC 8984-2245-1)

1. Introduction

Despite several remarkable exoplanet and brown dwarf discoveries by high-contrast imaging at high angular resolution in the past few years (e.g., Marois et al. 2008; Schmidt et al. 2008; Marois et al. 2010; Lagrange et al. 2010; Rameau et al. 2013; Bailey et al. 2014; Macintosh et al. 2015; Chauvin et al. 2017; Keppler et al. 2018; Haffert et al. 2019; Janson et al. 2019; Bohn et al. 2020a,b), there is an ongoing debate regarding the formation mechanisms that create these super-Jovian gas giants with semimajor axes greater than 10 au. It is unclear whether these companions have a star-like origin from a collapsing molecu-

⋆ Based on observations collected at the European Organisation for Astronomical Research in the Southern Hemisphere under ESO programs 099.C-0698(A), 0101.C-0153(A), 0101.C-0341(A), and 106.20X2.001.

lar cloud that is broken up into fragments, creating planetary-mass objects similar to a stellar binary (Kroupa 2001; Chabrier 2003), or through formation in a circumstellar disk instead. The classical bottom-up framework postulates formation via core accretion by coagulation of small dust grains into planetary embryos (Pollack et al. 1996; Alibert et al. 2005; Dodson-Robinson et al. 2009; Lambrechts & Johansen 2012). These evolve either via collisions or pebble accretion (Johansen & Lacerda 2010; Ormel & Klahr 2010) into planetary cores that are massive enough to accrete a gaseous envelope and to open a gap in the disk (Paardekooper & Mellema 2004). In the corresponding top-down scenario, planetary cores can be created by gravitational instabilities leading to the collapse of dense regions in the protoplanetary disk (Boss 1997; Rafikov 2005; Durisen et al. 2007; Kratter et al. 2010; Boss 2011; Kratter & Lodato 2016).

To study this question for the underlying planet formation mechanisms from a statistical point of view, several direct imaging surveys have been conducted (e.g., Vigan et al. 2012; Galicher et al. 2016; Bowler 2016; Vigan et al. 2017). Synthetic planet populations that represent each of the potential formation channels can be compared to the observational results from surveys and place constraints on the efficiency of the corresponding formation pathway (e.g., Mordasini et al. 2009a,b; Forgan & Rice 2013; Forgan et al. 2018). The two largest surveys were carried out with two of the most advanced adaptive-optics assisted, high-contrast imagers available: the Spectro-Polarimetric High-contrast Exoplanet REsearch (SPHERE; Beuzit et al. 2019) instrument at the 8.2 m ESO/VLT and the Gemini Planet Imager (GPI; Macintosh et al. 2014) at the 8.1 m Gemini South telescope. The preliminary statistical analysis of the first 300 stars from the Gemini PLanet Imager Exoplanet Survey (GPIES; Nielsen et al. 2019) concludes that giant planets between 10 au and 100 au that have masses smaller than 13 M_{Jup} favorably form via core accretion mechanisms, whereas brown dwarf companions in the same separation range but with masses from 13 M_{Jup} to 80 M_{Jup} seem to be predominantly created by disk instabilities. This finding is supported by the analysis of the first 150 stars observed within the scope of the SpHere INfrared survey for Exoplanets (SHINE; Vigan et al. 2020), which additionally hypothesizes that companions with masses between 1 M_{Jup} and 75 M_{Jup} are likely to originate from bottom-up formation scenarios around B and A type stars, whilst objects of the same mass around M-type stars are consistent with simulated populations from top-down mechanisms. For the intermediate masses of F-, G-, and K-type stars, the observed detections can be explained by a combination of both formalisms. A statistical meta-analysis on the distribution of wide-orbit companion eccentricities carried out by Bowler et al. (2020) provides supporting evidence for two distinct formation channels shaping the populations of giant planets ($2\,M_{\mathrm{Jup}} < M < 15\,M_{\mathrm{Jup}}$) and brown dwarfs ($15\,M_{\mathrm{Jup}} < M < 75\,M_{\mathrm{Jup}}$).

Most of these statistical evaluations are affected by the small number of actual substellar companions that were detected in the preceding imaging surveys. To expand the sample size for solar-mass host stars, we started the Young Suns Exoplanet Survey (YSES; Bohn et al. 2020a, Bohn et al. in prep.) that is observing a homogeneous sample of 70 ~15 Myr-old, K-type stars in the Lower Centaurus Crux (LCC) subgroup of the Scorpius-Centaurus association (Sco-Cen; de Zeeuw et al. 1999). All stars have masses close to 1 $M_{\odot}$ and the proximity (average parallactic distance $\langle D \rangle = 114 \pm 17$; Gaia Collaboration et al. 2020) and youth of the LCC facilitate the direct imaging search of giant, self-luminous substellar companions around these stars.

In this article we report the detection of a new exoplanet that was discovered within the scope of our survey. As this is already the second planetary system discovered by YSES, we introduce a new stellar identifier that is based on our survey acronym. The details of this new designation are described in §2. In §3 we describe our observations and data reduction methods. We discuss previous observations on the host star and reassess its main parameters in §4. The results of our high-contrast imaging observations are presented and analyzed in §5. We discuss potential formation mechanisms of this newly detected exoplanet in §6 and we present our conclusions in §7.

2. Nomenclature of YSES planets

Owing to the recent success of YSES, we decided to introduce a dedicated catalog that will be used for star-planet systems discovered within the scope of our survey. The YSES acronym has been verified by the IAU Commission B2 Working Group on Designations and was added to the Simbad database (Wenger et al. 2000).[1] The nomenclature of planet hosts from our survey is YSES NNN and planets that are associated with these stars will be named YSES NNNa, accordingly. Following these guidelines, we assigned the host star of the intriguing multi-planet system that was discovered around TYC 8998-760-1 the new primary identifier YSES 1 (Bohn et al. 2020a,b). The planets formerly known as TYC 8998-760-1 b and TYC 8998-760-1 c, will be named YSES 1b and YSES 1c, henceforth. Further planetary systems discovered by our survey will receive designated YSES identifiers followed by ascending integer identifications (IDs). Hence, the new companion discovered within the scope of this paper will be referred to as YSES 2b, orbiting its Sun-like host YSES 2.

3. Observations and data reduction

We observed YSES 2 (TYC 8984-2245-1, 2MASS J11275535-6626046) as part of YSES on the nights of 2018 April 30 (PI: Kenworthy) and 2020 December 8 (PI: Vogt) with SPHERE (mounted at the Nasmyth platform of Unit Telescope 3 of the ESO Very Large Telescope). We used the IRDIS camera (Dohlen et al. 2008) in classical imaging mode, applying a broadband filter in the H and K_s bands during the first and second nights, respectively. The observations were carried out in pupil stabilized imaging mode and an apodized Lyot coronagraph was used to block the flux of the primary star (Soummer 2005; Martinez et al. 2009; Carbillet et al. 2011). In addition to the science frames, we obtained center frames, with a sinusoidal pattern applied to the deformable mirror that creates a waffle pattern to locate the position of the star behind the coronagraphic mask; sky frames of an offset position with no adaptive optics (AO) correction and without any source in the field of view, to subtract the instrument and thermal background; and non-coronagraphic images of the star that are used for photometric reference of point sources detected in the science images. This last category of non-coronagraphic flux images was obtained with an additional neutral density filter in the optical path to record an unsaturated stellar point spread function (PSF) in the linear readout regime of the detector. This neutral density filter (filter ID: ND_1.0) provided an attenuation of 7.9 and 6.9 across the H and K_s bandpasses, respectively. A detailed description of the observing setup and the weather conditions can be found in Appendix A.

[1] Database entry available at: http://cds.u-strasbg.fr/cgi-bin/Dic-Simbad?/18721212

The data reduction was performed with PynPoint (version 0.8.1; Stolker et al. 2019) and included basic processing steps such as dark and flat calibration, bad pixel cleaning, sky subtraction, and correction for the instrumental distortion along the vertical axis of the detector. To remove the stellar halo that is affecting approximately the innermost 1″.2 around the coronagraph, we utilized an approach based on reference star differential imaging (RDI; Smith & Terrile 1984) in combination with principal component analysis (PCA; Amara & Quanz 2012; Soummer et al. 2012). As the parallactic rotation of our YSES observations is usually less than a few degrees, classical PSF subtraction schemes, such as angular differential imaging (ADI; Marois et al. 2006), perform much worse compared to this reference library approach. This method of combined RDI plus PCA was already successfully employed to recover circumstellar disks in archival HST data (e.g., Choquet et al. 2014) and within the scope of our survey for the discovery of a transition disk around the YSES target Wray 15-788 (Bohn et al. 2019).

Owing to the same location on sky, similar distances, and spectral types, all YSES targets exhibit very similar magnitudes in the red part of the optical spectrum (where the wavefront sensor of SPHERE is operating) and at the near-infrared wavelengths of our scientific observations. This facilitates comparable AO corrections amongst all our YSES observations, and the resulting images compose an excellent reference library to perform RDI. The reference targets that were used for our library PSF subtraction are listed in Appendix B. We modeled the stellar PSF with 50 principal components that were obtained from our full reference library. After the PSF subtraction, the frames were de-rotated according to their parallactic angles and median combined.

For the astrometric calibration we used the standard instrumental solution as presented by Maire et al. (2016) with a wavelength independent true north offset of $-1^\circ.75 \pm 0^\circ.08$ and plate scales of (12.251 ± 0.010) mas px^{-1} and (12.265 ± 0.010) mas px^{-1} in the H and K_s band, respectively.

4. Stellar properties

We briefly summarize previous literature characterizing YSES 2 in §4.1 and compile the stellar properties of YSES 2 in Table 1. In §4.2 and §4.3, we derive updated stellar parameters for YSES 2, more importantly, including stellar mass and age.

4.1. Previous studies

YSES 2 was first identified as a young star in the Search for Associations Containing Young stars (SACY) survey (Torres et al. 2006) of optical counterparts to the ROSAT All-Sky Survey (RASS) X-ray sources (Voges et al. 1999). Torres et al. (2006) reported the star to be a Li-rich (EW[Li I λ6707] = 367 mÅ) K1V(e) star with filled-in Hα, showing fast rotation ($v \sin i$ = 19.3 km s^{-1}) and radial velocity 15.8 ± 1.0 km s^{-1}. Based on its position, proper motion, and youth indicators, Preibisch & Mamajek (2008) included the star in a list of new members of the LCC subgroup of the Sco-Cen OB association (their Table 4), and provided initial estimates of isochronal age (16 Myr), mass (1.1 $M_\odot$), and fractional X-ray luminosity ($\log(L_X/L_{bol})$ = -3.2). Preibisch & Mamajek (2008) also predicted a kinematic distance of 109 pc (based on the proper motion and space velocity of LCC), which compares remarkably well to the Gaia EDR3 parallactic distance (ϖ = 9.1537 ± 0.0118 mas, D = 109.25 ± 0.14 pc; Gaia Collaboration et al. 2020). Kiraga (2012) reported the star to be a variable in the All Sky Automatic Survey (ASAS; IDed as ASAS J112755-6625.9) showing high amplitude (0.093 mag in V) and rapid rotation ($P_{\rm rot}$ = 2.7325 d), which is consistent with the observed saturated X-ray emission (and right near the median rotation period for Sco-Cen pre-main-sequence stars of $\langle P_{\rm rot}\rangle \simeq$ 2.4 d; Mellon et al. 2017). Pecaut & Mamajek (2016) include the star in their age analysis of pre-main-sequence K stars across Sco-Cen, estimating an age of 23 Myr and a mass of 1.0 $M_\odot$. The star has subsequently appeared in multiple LCC membership lists (Gagné et al. 2018; Goldman et al. 2018; Damiani et al. 2019). The status of this star as a pre-main-sequence member of LCC is strongly corroborated by a 99.9 % membership probability from the BANYAN Σ algorithm (Gagné et al. 2018) applied to the available *Gaia* astrometry and radial velocities (Gaia Collaboration et al. 2018, 2020).

4.2. Spectral analysis of YSES 2

To check the previously published spectral properties of YSES 2, we examined two archival UVES spectra from the ESO archive taken on UT 2007 May 2 (Program 079.C-0556(A); PI Torres). The UVES spectra at resolution R = 40,000 were convolved to lower resolution R = 3,000 and compared to the grid of MK spectral standards from Pecaut & Mamajek (2016). The blue spectrum, 3280 Å– 4560 Å, is consistent with K0V, but the red spectrum, 4730 Å– 6840 Å, appears to be K2V. The Hα line exhibits marginal emission, similar to the filled-in emission reported by Torres et al. (2006). Hence, we infer a temperature type of K1±1 and confirm the type K1V(e) published by Torres et al. (2006). From the original spectra, we independently measure the equivalent width of the Li I λ6707 feature to be 364 ± 5 mÅ, by simultaneously fitting Voigt profiles to the Li I feature and Fe I blend nearby (see, e.g., Soderblom et al. 1993). This is in good agreement with the 367 mÅ reported by Torres et al. (2006). The assigned luminosity class that we adapted from Torres et al. (2006) does not necessarily imply that YSES 2 is on the main sequence rather than being a pre-main-sequence star. Even though the luminosity and gravity indicators used by Torres et al. (2006) were more in line with main-sequence dwarfs than subgiant or giant standard stars, more persuasive indicators such as the HRD position, Li absorption, X-ray emission, and the confirmed LCC membership clearly favor the pre-main-sequence evolutionary stage.

4.3. Updated stellar parameters

Using the VOSA spectral energy distribution (SED) analyzer (Bayo et al. 2008),[2] we fit synthetic stellar spectra to the observed visible and infrared photometry for YSES 2. For priors, we constrained the reddening to be E($B-V$) = 0.016 ± 0.017 mag based on the STILISM 3D reddening maps (Lallement et al. 2019) and searched for best-fit synthetic spectra in the range 3000 K < $T_{\rm eff}$ < 6000 K, 3.5 dex < $\log g$ < 4.5 dex, and metallicities -0.5 < [Fe/H] < 0.5 and [α/Fe] = 0.0. A Bayesian fit using the BT-Settl-CIFIST models using 22 photometric points yielded the following parameters: A_V = 0.06 (0.02-0.09; 68%CL; 0.00-0.11; 95%CL), $T_{\rm eff}$ = 4749 K (4709-4789 K; 68%CL; 4700-4900 K; 95%CL), $\log g$ = 3.9 dex (3.5-4.5 dex), [Fe/H] = 0.0. We present the results of this SED fit in Fig. 1.

The best-fit bolometric flux is $f_{\rm bol}$ = (1.7490 ± 0.0248) ×10^{-9} erg s^{-1} cm^{-2}, which on the IAU 2015 apparent bolometric mag-

[2] Online available at: http://svo2.cab.inta-csic.es/theory/vosa/index.php

Table 1. Stellar properties of YSES 2.

Parameter	Value	Ref.
Main identifier	YSES 2	(1)
TYCHO ID	TYC 8984-2245-1	(2)
2MASS ID	J11275535-6626046	(3)
GAIA EDR3 ID	5236792880333011968	(4)
α (J2000) [hh mm ss.sss]	11 27 55.355	(4)
δ (J2000) [dd mm ss.ss]	-66 26 04.50	(4)
Spectral Type	K1V(e)	(5)
ϖ [mas]	9.1537 ± 0.0118	(4)
D [pc]	109.25 ± 0.14	(7)
$\mu_{\alpha*}$ [mas yr^{-1}]	-34.025 ± 0.013	(4)
μ_{δ} [mas yr^{-1}]	2.319 ± 0.011	(4)
$v_{\rm rad}$ [km s^{-1}]	13.41 ± 0.17	(5)
B [mag]	11.819 ± 0.010	(8)
V [mag]	10.860 ± 0.017	(8)
G [mag]	10.525 ± 0.003	(4)
I [mag]	9.773 ± 0.044	(9)
J [mag]	9.006 ± 0.026	(3)
H [mag]	8.484 ± 0.029	(3)
K_s [mag]	8.358 ± 0.029	(3)
$W1$ [mag]	8.323 ± 0.014	(10)
$W2$ [mag]	8.351 ± 0.008	(10)
$W3$ [mag]	8.258 ± 0.019	(11)
$W4$ [mag]	7.929 ± 0.118	(11)
P_{rot} [day]	2.7325	(9)
$v \sin i$ [km s^{-1}]	19.3 ± 0.5	(5)
$\log(L_X/L_{bol})$ [dex]	-3.07 ± 0.23	(9)
EW(Li I λ6707) [mÅ]	364 ± 0.05	(6)
EW(Hα) [mÅ]	0.0	(5)
U [km s^{-1}]	-10.10 ± 0.08	(7)
V [km s^{-1}]	-18.93 ± 0.12	(7)
W [km s^{-1}]	-5.60 ± 0.09	(7)
A_V [mag]	$0.06^{+0.03}_{-0.04}$	(6)
$T_{\rm eff}$ [K]	4749 ± 40	(6)
$m_{\rm bol}$ [mag]	10.396 ± 0.015	(6)
$M_{\rm bol}$ [mag]	5.204 ± 0.016	(6)
$\log(L/L_{\odot})$ [dex]	-0.1854 ± 0.0063	(6)
R [$R_{\odot}$]	1.193 ± 0.022	(6)
Mass [$M_{\odot}$]	1.10 ± 0.03	(6)
Age [Myr]	13.9 ± 2.3	(6)

References. (1) This paper, see §2; (2) Høg et al. (2000); (3) Cutri et al. (2003); (4) Gaia Collaboration et al. (2020), and *Gaia* EDR3 and DR2 ID #s are the same; (5) Torres et al. (2006); (6) this paper, see §4.3; (7) distance and heliocentric Galactic Cartesian velocity calculated using Gaia EDR3 values ($D = 1/\varpi$); (8) Henden et al. (2016); (9) Kiraga (2012); (10) Eisenhardt et al. (2020); (11) Cutri & et al. (2014).

nitude scale translates to $m_{\rm bol} = 10.396 \pm 0.015$ mag. Adopting the Gaia EDR3 parallax, this translates to absolute bolometric magnitude $M_{\rm Bol} = 5.204 \pm 0.016$ mag and bolometric luminosity $\log(L/L_{\odot}) = -0.1854 \pm 0.0063$. This is considerably more accurate than previous estimates ($\log(L/L_{\odot}) = -0.06$ (Preibisch & Mamajek 2008), $\log(L/L_{\odot}) = -0.265 \pm 0.075$ (Pecaut & Mamajek 2016)) and benefits from a very precise distance, well-constrained extinction from 3D reddening maps, and integrating synthetic SEDs using 22 photometric data points. Combining this improved luminosity estimate with the improved $T_{\rm eff}$ from the SED fitting ($T_{\rm eff} = 4749 \pm 40$ K) yields a good estimate of the radius of the star ($1.193 \pm 0.022\,R_{\odot}$). A comparison against evolutionary tracks from Baraffe et al. (2015) provided an updated stellar mass of $(1.10 \pm 0.03)\,M_{\odot}$ and an age of (13.9 ± 2.3) Myr. Furthermore we note that the SED of the star showed no signs of infrared excess through to the WISE-4 band (22 μm). The 2MASS-WISE colors (K_s-$W1$ = -0.035 ± 0.032 mag, K_s-$W2$ = -0.007 ± 0.030 mag, K_s-$W3$ = 0.100 ± 0.035 mag, K_s-$W4$ = 0.429 ± 0.122 mag) can be compared to the mean for K1 pre-main-sequence stars from Pecaut & Mamajek (2013) (K_s-$W1$ = 0.09 mag, K_s-$W2$ = 0.06 mag, K_s-$W3$ = 0.10 mag, K_s-$W4$ = 0.18 mag), and show a significant hint of IR excess. The K_s-$W4$ color is marginally red (2σ excess), perhaps hinting at a debris disk (common among non-accreting pre-main-sequence Sco-Cen stars), but there is no corroborating evidence to further support this.

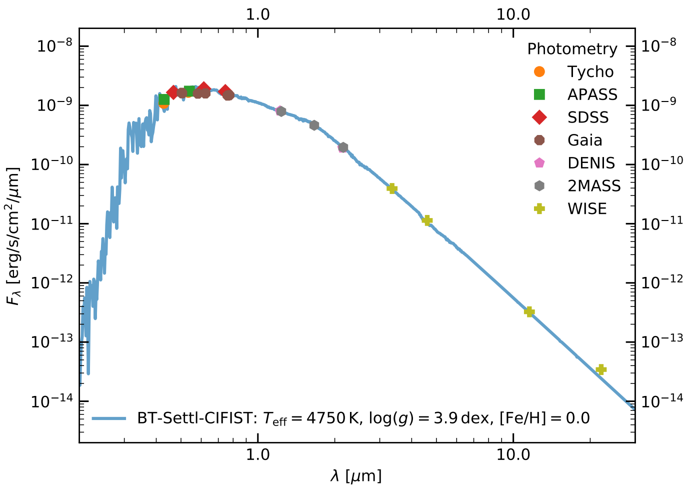


Fig. 1. Spectral energy distribution of YSES 2. The colored markers indicate the archival photometric measurements of the star and the blue curve presents our best-fit BT-Settl-CIFIST model to the data. The uncertainties of the photometric measurements are too small to be visualized in the figure.

We searched for common proper motion stellar or substellar companions for YSES 2. Assuming a mass of $1.0\,M_{\odot}$, the tidal radius of YSES 2 is ~1.35 pc (projected radius ~0°.71 or ~2560″; Mamajek et al. 2013), that is, bound companions would be expected to lie projected within this radius. Surveying the lists of Sco-Cen candidates and pre-main-sequence stars from the Gaia DR2 catalogs of Goldman et al. (2018), Zari et al. (2018), and Damiani et al. (2019) with parallactic distances of <140 pc shows only a couple of likely LCC siblings within 1° of YSES 2: the poorly studied classical T Tauri star Wray 15-813 at 2845″ (D = 101 pc) (Pereira et al. 2003) and uncharacterized candidate pre-main-sequence object 2MASS J11375287-6631197 (D = 104 pc). A query of the recently released Gaia EDR3 catalog searching for co-moving, co-distant objects (with generous selection range of proper motions in α and δ within ±5 mas yr^{-1}, and parallax ±2 mas of YSES 2) yields zero candidate companions within 1°. Thus far, YSES 2 appears to be a stellar singleton.

5. Observational results and analysis

In §5.1 we show that our observations reveal a co-moving companion to YSES 2. The reduced images for both epochs are presented in Fig. 2. Our photometric analysis in §5.2 indicates that this companion has a mass that is significantly lower than the deuterium burning limit of $\sim 13\,M_{\mathrm{Jup}}$. We refer to this newly identified planet as YSES 2b henceforth. In §5.3 we present the detection and mass limits of our acquired data.

5.1. Companion astrometry

We extracted the companion astrometry and photometry by the injection of negative artificial companions (e.g., Lagrange et al. 2010; Bonnefoy et al. 2011). A detailed description of our method is presented in Appendix C. The extracted astrometry is listed in Table 2. As visualized in the proper motion plot in Fig. 3 the companion is clearly incompatible with the calculated trajectory of a static background object at 14σ significance. The relative astrometric motion with respect to the primary is consistent with a comoving companion. This conclusion is further confirmed by a similar analysis of other point sources within the detector field of view. As presented in Appendix D, all additional off-axis point sources are consistent with being non-moving background contaminants. We thus conclude that YSES 2b is a gravitationally bound companion to its solar-mass host star. From our astrometric measurements we derived a projected physical separation of approximately 115 au. Future astrometric measurements are required to derive meaningful constraints to the orbital parameters of this wide-orbit planet.

5.2. Companion photometry

We present the photometry of the companion in Fig. 4 in a color-magnitude diagram. The corresponding numerical values are reported in Table 2. YSES 2b is consistent with a late L to early T spectral type when comparing it to colors of field brown dwarfs from the NIRSPEC Brown Dwarf Spectroscopic Survey (McLean et al. 2003, 2007), the IRTF spectral library (Rayner et al. 2009; Cushing et al. 2005), the L and T dwarf data archive Knapp et al. (2004); Golimowski et al. (2004); Chiu et al. (2006), and the SpeX Prism Libraries (Burgasser et al. 2010; Gelino & Burgasser 2010; Burgasser 2007; Siegler et al. 2007; Reid et al. 2006; Kirkpatrick et al. 2006; Cruz et al. 2004; Burgasser & McElwain 2006; McElwain & Burgasser 2006; Sheppard & Cushing 2009; Looper et al. 2007; Burgasser et al. 2008; Looper et al. 2010; Muench et al. 2007; Dhital et al. 2011; Kirkpatrick et al. 2010; Burgasser et al. 2004). Object distances were derived from Gaia EDR3 (Gaia Collaboration et al. 2020), the Brown Dwarf Kinematics Project (Faherty et al. 2009), and the Pan-STARRS1 3π Survey (Best et al. 2018). In color-magnitude space, YSES 2b is very close to the innermost three planets of the HR 8799 multi-planetary system (Marois et al. 2008, 2010). These three planets are classified as mid to late L type dwarfs (e.g., Greenbaum et al. 2018), which agrees well with the sequence evolution of the adjacent field brown dwarfs from L to T spectral types.[3] A similar spectral type in this domain, therefore, seems very likely for YSES 2b, requiring confirmation by measurements at higher spectral resolution. Whereas the masses of the spectrally similar trio of HR 8799 c, d, and e are in the range 7-12 M_{Jup} (Wang et al. 2018; Marois et al. 2008, 2010), it is likely that YSES 2b has an even lower mass as the system age of (13.9±2.3) Myr is significantly younger than the age of HR 8799, which is claimed to be member of the Columba association with an age of 30–50 Myr (Zuckerman et al. 2011; Bell et al. 2015). This is supported by the AMES-COND and AMES-dusty models (Allard et al. 2001; Chabrier et al. 2000) that we present in Fig. 4 for a system age of 13.9 Myr. An individual evaluation of these isochrones yielded masses from $5.3\,M_{\mathrm{Jup}}$ to $8.0\,M_{\mathrm{Jup}}$ as presented in Table 2. The uncertainties originate from the errors in the system age and planet magnitude that were propagated by a bootstrapping approach with 1,000 randomly drawn samples from Gaussian distributions around both parameters. When combining the posterior distributions for the different models and filters we derived a final mass estimate of $6.3^{+1.6}_{-0.9}\,M_{\mathrm{Jup}}$ as the 68% confidence interval around the median of the sample. This estimate is based on broadband photometric measurements alone; further spectral coverage of the planetary SED will be important to constrain its effective temperature, luminosity, surface gravity, and mass.

5.3. Detection limits

To derive upper mass limits for additional companions in the system, we calculated the detection limits of our datasets. As a baseline, we evaluated the contrast in the image that was obtained by de-rotating and median combining the individual exposures without any PSF subtraction. This image covers the full field of view of the SPHERE/IRDIS detector up to an angular separation of 5$''$.5. We evaluated the contrast directly in the final image using aperture photometry. The chosen aperture size was one full width at half maximum (FWHM) of the unsaturated stellar PSF as measured in the flux images (see Table A.1 in Appendix A). The signal flux was measured as the sum over the full circular aperture within the mean combined flux image and scaled for the flux difference with the science frames owing to the shorter exposure times and the applied neutral density filters. For several radial positions that were equidistantly sampled from 0$''$.15 to 5$''$.50 in steps of 0$''$.05, we measured the noise as the standard deviation of the integrated flux within apertures that were distributed around the star at the same radial separation (excluding the signal aperture itself). We applied a sigma clipping with an upper bound of 3σ to the integrated fluxes of the noise apertures before calculating the standard deviation to discard apertures that were polluted by flux of off-axis point sources (see the full frame image in Fig. D.1 in Appendix D). A correction for small sample statistics as described in Mawet et al. (2014) was considered in these noise calculations. We reiterated this analysis for six uniformly spaced position angles and present the azimuthally averaged results as two-dimensional contrast curves in Fig. 5. The solid yellow lines represent the 5σ raw contrast in the H and K_s bands that was obtained without any PSF subtraction.

For the innermost region around the star (< 1$''$.2), the sensitivity was additionally assessed considering our PSF subtraction by RDI plus PCA. We used the `ContrastCurveModule` from `PynPoint` version 0.6.0[4] that utilizes the same aperture pho-

[3] We would like to note that the planets around HR 8799, although closely located to the sequence of field brown dwarfs in the selected SPHERE filters as presented in the color-magnitude diagram in Fig. 4, can have near-infrared colors in different passbands that are significantly distinct from those of their field dwarf analogs (e.g., Currie et al. 2011).

[4] As mentioned before, version 0.8.1 of `PynPoint` was used for all remaining analysis steps. The modules of both versions are compatible; only the implementation of some algorithms changed throughout the development process. This affects the `ContrastCurveModule`, which follows the iterative process described in this paragraph for release ver-

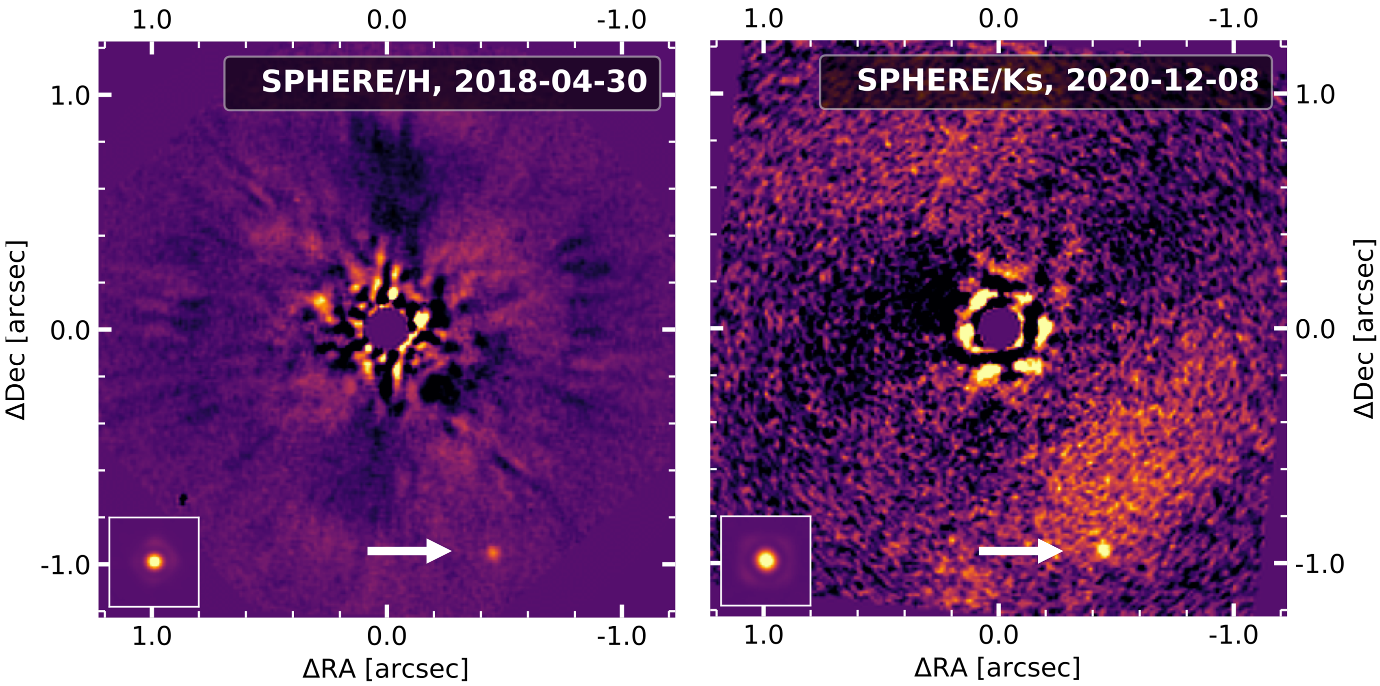


Fig. 2. Multi-epoch observations of YSES 2 and its planetary-mass companion. Final data products of the SPHERE observations collected in the H band (left panel) and K_s band (right panel) are presented. For both filters, the stellar PSF is modeled by 50 principal components that were derived from a reference library of YSES targets. These PSF models were subtracted and the residuals rotated such that north points up and east toward the left. In the presented images the median of these de-rotated residuals is shown. For the K_s band data, uncorrected residuals of a wind-driven halo are detected that extend from the northeast to southwest. The planet YSES 2b is highlighted by white arrows. The primary is located at the origin of the coordinate system and we artificially masked the inner region up to the radial extent of the coronagraphic mask of 100 mas. To assess the spatial extent of the instrumental PSF, the median combination of the non-coronagraphic flux images of the primary star are shown in the lower left of each panel. The intensity of each flux image is rescaled to match the maximum and minimum counts in the corresponding residual science image, and we display both images with the same spatial and color scales.

Table 2. Astrometry, photometry, and derived masses of YSES 2b.

Observation date	Filter	Separation	Position angle	ΔMag	M_{abs}	Photometric mass	
						COND	Dusty
(yyyy-mm-dd)		(mas)	(°)	(mag)	(mag)	(M_{Jup})	(M_{Jup})
2018-04-30	H	1057 ± 3	205.3 ± 0.2	10.37 ± 0.11	13.57 ± 0.11	5.3 ± 0.5	8.0 ± 0.7
2020-12-08	K_s	1053 ± 5	205.2 ± 0.2	9.55 ± 0.11	12.71 ± 0.11	6.1 ± 0.6	6.4 ± 0.6

tometry framework and metric to evaluate the contrast for several positions that were distributed around the star in the residual images. For each position, the module injects an artificial companion, whose detection significance is evaluated after the PSF subtraction with RDI combind with PCA. In this framework, the signal aperture is directly placed on top of the position at which the artificial companion has been injected, and the noise apertures are azimuthally distributed around the primary star as described before, yet excluding the signal aperture itself. The companion template was obtained as the median combination of the non-coronagraphic flux images that was scaled for the difference in exposure time and the attenuation due to the applied neutral density filter. From an initial magnitude contrast of 8 mag, the flux of the injected companion was adjusted and the post-processing was performed iteratively until the artificial companion was retrieved at 5σ detection significance in the final image product. These limiting magnitude contrasts were stored for each of the injection positions. For the calculation of the final contrast curves with RDI plus PCA, we used a radial sampling in the range 0.″15-1.″20 with a spatial resolution of 0.″05, and six position angles that were equidistantly sampled in polar space. Again, the contrast as a function of radial separation was obtained by azimuthal averaging of the various position angles. We considered several numbers of principal components to model the stellar PSF as indicated by the sequentially colored, dashed lines in Fig. 5. The detectable planet masses that correspond to the calculated magnitude contrasts were derived by evaluation of AMES-COND models at the system age of 13.9 Myr (see right axes of Fig. 5).

The contrast performance close the star improves for an increasing number of principal components. This differential gain in contrast ceases for ~50 subtracted components and the contrast for 100 principal components does not change significantly compared to the curve generated for half as many components. This justifies our previously selected value of 50 principal components that were used for our PSF subtraction with RDI plus PCA. This amount of components is equivalent to 19 % and 30 % of the reference libraries in the H and K_s bands, which are com-

sion 0.6.0. We prefer this implementation over the solution presented in `PynPoint` version 0.8.1, which calculates one attenuation factor per position that is based on the single injection of an artificial companion with a user-defined signal-to-noise ratio.

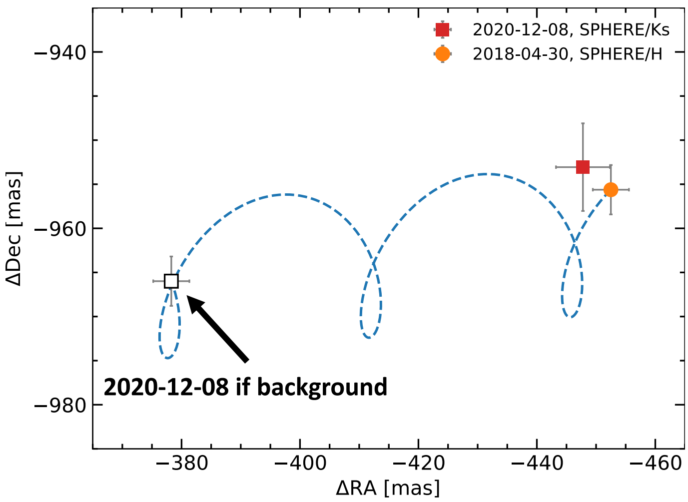


Fig. 3. Proper motion plot for YSES 2b. The colored markers represent the relative astrometry with respect to the primary star measured for our two observational epochs. The blue trajectory indicates the simulated motion of a static background object at infinity and the white marker is the theoretical position of such an object at our second observational epoch.

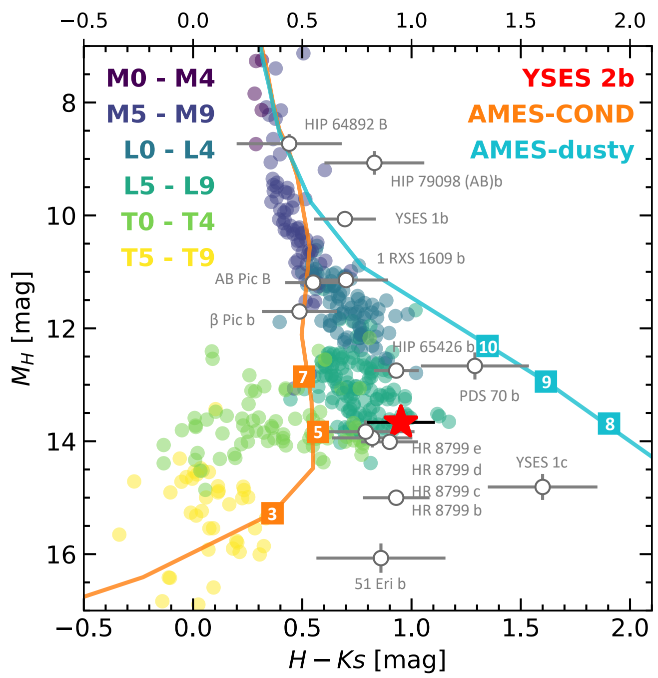


Fig. 4. Color-magnitude diagram for YSES 2b. The colored markers show the sequence of field brown dwarfs with various spectral types from M to late T. The white markers represent known directly imaged companions that are usually younger than the presented field objects. YSES 2b is highlighted by the red star. We further show AMES-COND and AMES-dusty evolutionary models that were evaluated at a system age of 13.9 Myr (solid lines). The markers along the line indicate the equivalent object masses in $M_{\rm Jup}$.

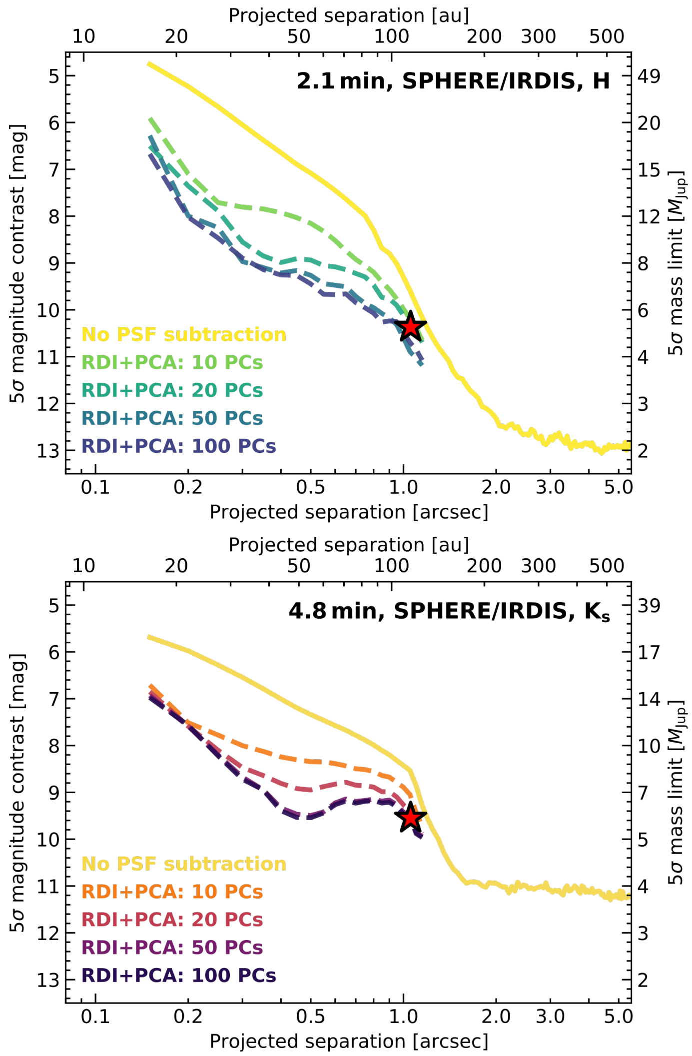


Fig. 5. 5σ detection limits of our SPHERE/IRDIS observations in the H (upper panel) and K_s bands (lower panel). On the left axis the magnitude contrast with respect to the primary star is reported, and the absolute magnitudes are converted to detectable planet masses with AMES-COND models as indicated on the right axis; this scale varies between the H and K_s bands. The solid yellow lines represent the limits when no PSF subtraction is performed. The dashed lines indicate the sensitivity, when a PSF subtraction with RDI plus PCA is performed. The red star highlights the contrast of YSES 2b that we detect at ∼ 5σ significance in both filters after PSF subtraction with more than 50 principal components.

posed of 269 and 164 individual frames, respectively. In the H band we observe a contrast improvement of more than two magnitudes at an angular separation of 0$''$.2. This corresponds to an increase in planet detection sensitivity by more than 45 $M_{\rm Jup}$ at this close separation. The contrast improvement in the H band is maximized at an angular separation of ∼0$''$.3, where RDI plus PCA provides detection limits that are approximately three magnitudes deeper than our raw data. At angular separations larger than 1$''$ the contrast improvement decreases as the flux contribution of the stellar PSF becomes negligible. At separations ≥ 2$''$ we reach a fundamental noise floor that is mainly composed of residual sky background and detector read out noise. The K_s band contrast behaves very similar to the detection limits in the H band and the RDI plus PCA reduction scheme can provide a maximum gain of up to 2.5 mag at an angular separation of ∼0$''$.4. The overall improvement for separations < 1$''$ is marginally worse compared to the H band data and the contribution of the asymmetric wind-driven halo is clearly visible for separations in the range 0$''$.5-1$''$.2. Combining the data from the H and K_s bands allows us to exclude stellar and brown dwarf companions around YSES 2 with masses > 13 $M_{\rm Jup}$ for angular separations that are larger than 0$''$.15. At 0$''$.5 we are sensitive to objects that are more massive than 6 $M_{\rm Jup}$ and for angular sepa-

rations that are larger than 2″ we can even rule out planets with masses as low as 2 $M_{\rm Jup}$.

This demonstrates, impressively, how a large reference library can help to significantly improve the contrast performance at small angular separations < 1.″2. Especially for datasets with little parallactic rotation, RDI plus PCA should be considered as a default PSF subtraction strategy. This conclusion is also supported by first results from the star-hopping mode that was recently implemented at VLT/SPHERE (Wahhaj et al. 2021). As visualized by the red stars in Fig. 5, RDI plus PCA is required to detect YSES 2b at 5σ significance in both the H and K_s band data.

6. Discussion

The newly discovered planetary companion to YSES 2 is among the lowest mass direct imaging companions known to date. The only objects of similar low mass are 51 Eri b (Macintosh et al. 2015), HD 95086 b (Rameau et al. 2013), HR8799 b (Marois et al. 2008), PDS 70 b and c, (Keppler et al. 2018; Haffert et al. 2019; Wang et al. 2020; Stolker et al. 2020a), and YSES 1c (Bohn et al. 2020b). Of these, only YSES 1c is located around a solar-mass star. Within the uncertainties, the mass of YSES 2b is the same as YSES 1c, which we previously discovered in our survey. Given our mass estimate for the planet, the mass ratio of YSES 2b to its host star is $q = 0.54^{+0.13}_{-0.08}$ %. This value is comparable, but slightly lower than the $q = 0.57 \pm 0.10$ % derived for YSES 1c. The mass ratio is the lowest among direct imaging companions to solar-type stars.[5]

The in situ formation of super-Jovian planets at tens or hundreds of Astronomical Units is challenging. We recently discussed possible formation scenarios for such objects in the context of the YSES 1 system in Bohn et al. (2020a). In our previous study we considered scattering or planet capturing events to explain the current large separation of YSES 1b. However, dynamic scattering by a third body in the system is expected to produce high eccentricities, inconsistent with orbital stability of both planetary components in the YSES 1 system (Bohn et al. 2020b).[6] The new detection of YSES 2b in our small survey sample of 70 solar-type systems in Sco-Cen makes the hypothesis that we see captured free-floating planets unlikely. Goulinski & Ribak (2018) find with numerical simulations that only ∼0.1% of solar-type stars in the Galactic thin disk should capture a free-floating planet in their lifetime. YSES 2b in principle might have formed in situ via disk gravitational instability. Boss (2011) find that they can produce 1-5 $M_{\rm Jup}$ planets between 30 au and 70 au with eccentricities as high as 0.35. If YSES 2b is on an eccentric orbit it may explain its current projected separation of 110 au. Kratter et al. (2010) conversely find with their hydrodynamic simulations that planets formed via disk instability need to be at large separations outside of the 40 au to 70 au range to not accumulate too much mass and remain in the planetary regime. This hypothesis that gravitationally instabilities predominantly create brown dwarf and stellar companions is supported by other theoretical studies (e.g., Zhu et al. 2012; Forgan & Rice 2013). Spatially resolved observations of gas-rich planet forming disks in the last few years have shown that radial substructures, which are thought to be caused by perturbing planets, are nearly ubiquitous (see, e.g., Garufi et al. 2018 for an overview, observed in scattered light). These structures can, in a growing number of cases, be traced out to tens or hundreds of Astronomical Units (e.g., ALMA Partnership et al. 2015; Ginski et al. 2016; de Boer et al. 2016; van Terwisga et al. 2018). Recently it was found that these substructures are already present in protostellar disks as young as ∼0.1 Myr (Sheehan et al. 2020; Sheehan 2020), suggesting that planet formation sets in early and operates on short timescales. Despite this abundance of substructures observed in young, circumstellar environments, it is unlikely that all these protoplanetary disks are gravitationally unstable and support planet formation via this channel (e.g., Kratter & Lodato 2016). Conversely, we expect that the timescale to form a planet via core accretion at the current location of YSES 2b would be too long, given the system age and that the gas-rich disk in the system has already dissipated (e.g., Haisch et al. 2001).

Even though capturing scenarios are considered unlikely for YSES 2b, we cannot confidently conclude whether its formation via either top-down or bottom-up scenarios is more likely: whereas a mass of 6.3 $M_{\rm Jup}$ is rather low for an object to originate from gravitational disk instabilities, core accretion would favor a formation at closer separations to the star. More data are thus required to explore the origin of this wide-orbit Jovian giant. Promising methods to evaluate the likelihood of either formation scenario are by characterization measurements of the planetary atmosphere, continuous orbital monitoring to constrain especially its eccentricity, and deeper searches for additional companions in the system.

To identify the formation channel of YSES 2b via atmospheric characterization, we can utilize the framework postulated by Öberg et al. (2011), who argued that elemental abundances in the planetary atmosphere (and especially the C/O ratio) are directly linked to its natal environment in the planet-forming disk. Different ice lines in the protoplanetary disk and the associated freeze out of the corresponding molecular species alter molecular abundance ratios as a function of radial separation from the host star, making this atmospheric quantity a promising indicator of the natal environment and formation channel of a planet. The chemical and dynamical evolution of the disk can alter these initial abundances and should be considered in the analysis (e.g., Ali-Dib et al. 2014; Mordasini et al. 2016; Eistrup et al. 2016, 2018). Gravity Collaboration et al. (2020) utilized this framework to study β Pic b and proposed its formation through core accretion, with strong planetesimal enrichment based on its subsolar C/O abundance ratio. If YSES 2b formed via disk gravitational instability, then we expect this object to have similar elemental abundances as the primary star in the system, while formation by core accretion should lead to an over-abundance of heavy elements due to pebble accretion. YSES 2b, along with other planet mass objects detected by direct imaging, provides an ideal test case for future detailed atmospheric characterization.

We can further continue to monitor the separation and position angle of YSES 2b with respect to the primary star to derive orbital solutions for the planet (e.g., Wang et al. 2018). In particular, the VLTI/GRAVITY instrument (Gravity Collaboration et al. 2017) will be extremely useful for this purpose, as it facilitates an unprecedented astrometric precision down to submilliarcsecond scales (e.g., Gravity Collaboration et al. 2019; Wang et al. 2021). These astrometry measurements could be complemented by VLT/CRIRES$^+$ data to constrain the radial velocity of the planet and to obtain three-dimensional information about its orbital motion (e.g., Schwarz et al. 2016). The eccentricity of the planet might provide hints regarding the likelihood of a potential migration of the companion, which would be an

[5] See Bohn et al. (2020a) for an overview of mass ratios of direct imaging companions to solar-type stars.

[6] We, however, note that in some cases high eccentricities are inferred for substellar companions, for example, the brown dwarf companion to the young solar analog PZ Tel (Mugrauer et al. 2012; Ginski et al. 2014).

indicator of formation via core accretion at closer separation to the star. If this migration was caused by scattering off another, so far undetected companion to the primary star, a deep imaging campaign is required to search for evidence of such an additional component to the planetary system. At the moment, we cannot provide conclusive evidence for the most likely formation scenario of YSES 2b based on the available data; but future observations might be able to shed light on the origin of this Jovian gas giant.

Even though the second epoch observations of YSES are not concluded yet and candidate companions to ∼45 stars of our sample need to be confirmed or rejected, our survey has already discovered three planetary-mass companions amongst 70 young, Sun-like stars. This high planet-detection rate is in stark contrast to previous surveys that were targeting Sun-like stars at closer distances than the LCC (e.g., Kasper et al. 2007; Biller et al. 2013; Galicher et al. 2016), which discovered mostly stellar and brown dwarf companions. These preliminary statistical results from YSES tentatively indicate that despite the farther distance, Sco-Cen and especially LCC are more favorable than moving groups in the immediate solar neighborhood for the detection of young planets briefly after their formation. Many of the moving groups that were targeted in these aforementioned surveys are significantly older than LCC (15 ± 3 Myr), such as the Tucana-Horologium moving group (45 ± 4 Myr Bell et al. 2015), the AB Dor moving group (149^{+51}_{-19} Myr; Bell et al. 2015), or the Hercules-Lyra association (257 ± 46 Myr; Eisenbeiss et al. 2013). As a consequence of the decreasing luminosity of objects below the deuterium burning limit with increasing age (e.g., Burrows et al. 1997), it is natural that the sensitivity to Jovian planets is worse around members of these associations compared to significantly younger host stars. Yet some of these closer moving groups have ages comparable to that of LCC – such as the TW Hya association (10 ± 3 Myr) or the β Pic moving group (24 ± 3 Myr; Bell et al. 2015) – and should provide even better planet-detection sensitivities owing to their much closer distances. However, before speculating about potential reasons for this tentative overabundance of planetary-mass companions to our YSES targets, it is necessary to finish the second epoch observations of the survey and to derive reliable occurrence rates of planetary-mass companions to Sun-like stars in Sco-Cen.

7. Conclusions

We report the detection of a new directly imaged planet to the solar-mass primary YSES 2 that was discovered within the scope of YSES. Reassessment of the stellar parameters provided an effective temperature of $T_{\text{eff}} = (4749 \pm 40)$ K, a luminosity of $\log(L/L_\odot) = -0.1854 \pm 0.0063$, a mass of $(1.10 \pm 0.03)\, M_\odot$, and a system age of (13.9 ± 2.3) Myr.

We detect YSES 2b in two consecutive epochs collected on 2018 April 30 and 2020 December 18 with VLT/SPHERE. The companion has a projected separation of approximately 1.″05, which translates to a physical minimum distance of ∼115 au with respect to the primary star. Photometric measurements in the H and K_s bands constrain a planet mass of $6.3^{+1.6}_{-0.9}\, M_{\text{Jup}}$ according to AMES-COND and AMES-dusty evolutionary models. This mass estimate is supported by the position of the object in color-magnitude space, where it is located amongst the mid to late L type field brown dwarfs and close to HR 8799 c, d, and e. The slightly higher mass estimates of these exoplanets on the order of 7–12 M_{Jup} are consistent with the older system age of HR 8799 of 30–50 Myr.

The mass and separation of YSES 2b are inconsistent with planet populations for most in situ formation scenarios: whereas disk instabilities predominantly create companions above the deuterium burning limit at a separation of 110 au, core-accretion mechanisms are not efficient enough to form a planet of 6.3 M_{Jup} this widely separated from the primary star. So, the new companion might be either at the low-mass end of potential in situ formation outcomes from top-down scenarios, or it formed via core accretion at closer separation to the star and migrated to its current location. Atmospheric characterization measurements of molecular abundance ratios, orbital monitoring, and evaluation of the eccentricity of the planet, or a deep search for additional companions in the system, might help to evaluate the likelihood of these potential formation pathways. While we cannot rule out scattering or capture scenarios, we point out that the former require an (as of yet) third undetected body in the system, while the latter are unlikely given numerical simulations. YSES 2b is an important addition to the sparsely populated group of wide-orbit gas giant companions. Owing to the moderate separation with respect to the primary star, spectroscopic observations with JWST, VLT/ERIS, or VLTI/GRAVITY will be easily available. These data will be important to further constrain the properties of this Jovian companion. Measurements of molecular abundance ratios such as C/O or its orbital eccentricity might even facilitate hypotheses regarding the most likely formation mechanism for this wide-orbit gas giant planet.

Our data rule out brown dwarf and stellar companions with $M > 13\, M_{\text{Jup}}$ in the SPHERE/IRDIS field of view for angular separations > 0.″15 and at 0.″5 we can exclude objects that are more massive than 6 M_{Jup} . At separations that are larger than 2″ we are even sensitive to planets with masses as low as 2 M_{Jup} . In general, the applied PSF subtraction scheme based on RDI plus PCA is extremely successful and provides substantial contrast improvements (> 1 mag) for separations that are smaller than 1″. In the H band, the PSF subtraction enhances our sensitivity by more than 45 M_{Jup} at 0.″2, and the greatest contrast improvement of ∼3 mag is achieved at an angular separation of 0.″3. Our YSES strategy with short snapshot observations of ≤ 5 min combined with a large reference library for PSF subtraction is certainly a promising approach to image planetary-mass companions to young, Sun-like stars in Sco-Cen. With three newly discovered planetary-mass companions in less than 40 h of allocated telescope time the survey efficiency is unprecedented and the mission concept can certainly be applied to future high-contrast imaging studies targeting different samples of pre-main-sequence stars.

Acknowledgements. We would like to thank the anonymous referee for the very valuable feedback that helped improving the quality of the manuscript. Especially, the extremely kind way of providing this feedback was highly appreciated by the authors. The research of AJB and FS leading to these results has received funding from the European Research Council under ERC Starting Grant agreement 678194 (FALCONER). Part of this research was carried out at the Jet Propulsion Laboratory, California Institute of Technology, under a contract with the National Aeronautics and Space Administration (80NM0018D0004). MM would like to thank the German Research Foundation (DFG) for support in the program MU 2695/27-1. CA acknowledges support by ANID – Millennium Science Initiative Program – NCN19_171. MR acknowledges support from the FWO research program under project 1280121N. This research has used the SIMBAD database, operated at CDS, Strasbourg, France (Wenger et al. 2000). This work has used data from the European Space Agency (ESA) mission *Gaia* (https://www.cosmos.esa.int/gaia), processed by the *Gaia* Data Processing and Analysis Consortium (DPAC, https://www.cosmos.esa.int/web/gaia/dpac/consortium). Funding for the DPAC has been provided by national institutions, in particular the institutions participating in the *Gaia* Multilateral Agreement. This publication makes use of VOSA, developed under the Spanish Virtual Observatory project supported by the Spanish MINECO through grant AyA2017-84089. To achieve the scientific results presented in this article

we made use of the *Python* programming language[7], especially the *SciPy* (Virtanen et al. 2020), *NumPy* (Oliphant 2006), *Matplotlib* (Hunter 2007), *emcee* (Foreman-Mackey et al. 2013), *scikit-image* (Van der Walt et al. 2014), *scikit-learn* (Pedregosa et al. 2012), *photutils* (Bradley et al. 2016), and *astropy* (Astropy Collaboration et al. 2013, 2018) packages.

References

Ali-Dib, M., Mousis, O., Petit, J.-M., & Lunine, J. I. 2014, ApJ, 785, 125
Alibert, Y., Mordasini, C., Benz, W., & Winisdoerffer, C. 2005, A&A, 434, 343
Allard, F., Hauschildt, P. H., Alexander, D. R., Tamanai, A., & Schweitzer, A. 2001, ApJ, 556, 357
ALMA Partnership, Brogan, C. L., Pérez, L. M., et al. 2015, ApJ, 808, L3
Amara, A. & Quanz, S. P. 2012, MNRAS, 427, 948
Astropy Collaboration, Price-Whelan, A. M., Sipőcz, B. M., et al. 2018, AJ, 156, 123
Astropy Collaboration, Robitaille, T. P., Tollerud, E. J., et al. 2013, A&A, 558, A33
Bailey, V., Meshkat, T., Reiter, M., et al. 2014, ApJ, 780, L4
Baraffe, I., Homeier, D., Allard, F., & Chabrier, G. 2015, A&A, 577, A42
Bayo, A., Rodrigo, C., Barrado Y Navascués, D., et al. 2008, A&A, 492, 277
Bell, C. P. M., Mamajek, E. E., & Naylor, T. 2015, MNRAS, 454, 593
Best, W. M. J., Magnier, E. A., Liu, M. C., et al. 2018, ApJS, 234, 1
Beuzit, J. L., Vigan, A., Mouillet, D., et al. 2019, A&A, 631, A155
Biller, B. A., Liu, M. C., Wahhaj, Z., et al. 2013, ApJ, 777, 160
Bohn, A. J., Kenworthy, M. A., Ginski, C., et al. 2019, A&A, 624, A87
Bohn, A. J., Kenworthy, M. A., Ginski, C., et al. 2020a, MNRAS, 492, 431
Bohn, A. J., Kenworthy, M. A., Ginski, C., et al. 2020b, ApJ, 898, L16
Bonnefoy, M., Lagrange, A. M., Boccaletti, A., et al. 2011, A&A, 528, L15
Boss, A. P. 1997, Science, 276, 1836
Boss, A. P. 2011, ApJ, 731, 74
Bowler, B. P. 2016, PASP, 128, 102001
Bowler, B. P., Blunt, S. C., & Nielsen, E. L. 2020, AJ, 159, 63
Bradley, L., Sipocz, B., Robitaille, T., et al. 2016, Photutils: Photometry tools
Burgasser, A. J. 2007, ApJ, 659, 655
Burgasser, A. J., Cruz, K. L., Cushing, M., et al. 2010, ApJ, 710, 1142
Burgasser, A. J., Liu, M. C., Ireland, M. J., Cruz, K. L., & Dupuy, T. J. 2008, ApJ, 681, 579
Burgasser, A. J. & McElwain, M. W. 2006, AJ, 131, 1007
Burgasser, A. J., McElwain, M. W., Kirkpatrick, J. D., et al. 2004, AJ, 127, 2856
Burrows, A., Marley, M., Hubbard, W. B., et al. 1997, ApJ, 491, 856
Cantalloube, F., Por, E. H., Dohlen, K., et al. 2018, A&A, 620, L10
Carbillet, M., Bendjoya, P., Abe, L., et al. 2011, Experimental Astronomy, 30, 39
Chabrier, G. 2003, PASP, 115, 763
Chabrier, G., Baraffe, I., Allard, F., & Hauschildt, P. 2000, ApJ, 542, 464
Chauvin, G., Desidera, S., Lagrange, A. M., et al. 2017, in SF2A-2017: Proceedings of the Annual meeting of the French Society of Astronomy and Astrophysics, Di
Chiu, K., Fan, X., Leggett, S. K., et al. 2006, AJ, 131, 2722
Choquet, E., Hagan, J. B., Pueyo, L., et al. 2014, in Exploring the Formation and Evolution of Planetary Systems, Vol. 299, 30–31
Cruz, K. L., Burgasser, A. J., Reid, I. N., & Liebert, J. 2004, ApJ, 604, L61
Currie, T., Burrows, A., Itoh, Y., et al. 2011, ApJ, 729, 128
Cushing, M. C., Rayner, J. T., & Vacca, W. D. 2005, ApJ, 623, 1115
Cutri, R. M. & et al. 2014, VizieR Online Data Catalog, II/328
Cutri, R. M., Skrutskie, M. F., van Dyk, S., et al. 2003, 2MASS All Sky Catalog of point sources. (IPAC)
Damiani, F., Prisinzano, L., Pillitteri, I., Micela, G., & Sciortino, S. 2019, A&A, 623, A112
de Boer, J., Salter, G., Benisty, M., et al. 2016, A&A, 595, A114
de Zeeuw, P. T., Hoogerwerf, R., de Bruijne, J. H. J., Brown, A. G. A., & Blaauw, A. 1999, AJ, 117, 354
Dhital, S., Burgasser, A. J., Looper, D. L., & Stassun, K. G. 2011, AJ, 141, 7
Dodson-Robinson, S. E., Veras, D., Ford, E. B., & Beichman, C. A. 2009, ApJ, 707, 79
Dohlen, K., Langlois, M., Saisse, M., et al. 2008, in Proc. SPIE, Vol. 7014, Ground-based and Airborne Instrumentation for Astronomy II, 70143L
Durisen, R. H., Boss, A. P., Mayer, L., et al. 2007, in Protostars and Planets V, ed. B. Reipurth, D. Jewitt, & K. Keil, 607
Eisenbeiss, T., Ammler-von Eiff, M., Roell, T., et al. 2013, A&A, 556, A53
Eisenhardt, P. R. M., Marocco, F., Fowler, J. W., et al. 2020, ApJS, 247, 69
Eistrup, C., Walsh, C., & van Dishoeck, E. F. 2016, A&A, 595, A83
Eistrup, C., Walsh, C., & van Dishoeck, E. F. 2018, A&A, 613, A14
Faherty, J. K., Burgasser, A. J., Cruz, K. L., et al. 2009, AJ, 137, 1
Foreman-Mackey, D., Hogg, D. W., Lang, D., & Goodman, J. 2013, PASP, 125, 306
Forgan, D. & Rice, K. 2013, MNRAS, 432, 3168
Forgan, D. H., Hall, C., Meru, F., & Rice, W. K. M. 2018, MNRAS, 474, 5036
Gagné, J., Mamajek, E. E., Malo, L., et al. 2018, ApJ, 856, 23
Gaia Collaboration, Brown, A. G. A., Vallenari, A., et al. 2018, A&A, 616, A1
Gaia Collaboration, Brown, A. G. A., Vallenari, A., et al. 2020, arXiv e-prints, arXiv:2012.01533
Galicher, R., Marois, C., Macintosh, B., et al. 2016, A&A, 594, A63
Garufi, A., Benisty, M., Pinilla, P., et al. 2018, A&A, 620, A94
Gelino, C. R. & Burgasser, A. J. 2010, AJ, 140, 110
Ginski, C., Mugrauer, M., Seeliger, M., et al. 2016, MNRAS, 457, 2173
Ginski, C., Schmidt, T. O. B., Mugrauer, M., et al. 2014, MNRAS, 444, 2280
Goldman, B., Röser, S., Schilbach, E., Moór, A. C., & Henning, T. 2018, ApJ, 868, 32
Golimowski, D. A., Leggett, S. K., Marley, M. S., et al. 2004, AJ, 127, 3516
Goulinski, N. & Ribak, E. N. 2018, MNRAS, 473, 1589
Gravity Collaboration, Abuter, R., Accardo, M., et al. 2017, A&A, 602, A94
Gravity Collaboration, Lacour, S., Nowak, M., et al. 2019, A&A, 623, L11
Gravity Collaboration, Nowak, M., Lacour, S., et al. 2020, A&A, 633, A110
Greenbaum, A. Z., Pueyo, L., Ruffio, J.-B., et al. 2018, AJ, 155, 226
Haffert, S. Y., Bohn, A. J., de Boer, J., et al. 2019, Nature Astronomy, 3, 749
Haisch, Karl E., J., Lada, E. A., & Lada, C. J. 2001, ApJ, 553, L153
Henden, A. A., Templeton, M., Terrell, D., et al. 2016, VizieR Online Data Catalog, II/336
Høg, E., Fabricius, C., Makarov, V. V., et al. 2000, A&A, 355, L27
Hunter, J. D. 2007, Computing in Science and Engineering, 9, 90
Janson, M., Asensio-Torres, R., André, D., et al. 2019, A&A, 626, A99
Johansen, A. & Lacerda, P. 2010, MNRAS, 404, 475
Kasper, M., Apai, D., Janson, M., & Brandner, W. 2007, A&A, 472, 321
Keppler, M., Benisty, M., Müller, A., et al. 2018, A&A, 617, A44
Kiraga, M. 2012, Acta Astron., 62, 67
Kirkpatrick, J. D., Barman, T. S., Burgasser, A. J., et al. 2006, ApJ, 639, 1120
Kirkpatrick, J. D., Looper, D. L., Burgasser, A. J., et al. 2010, ApJS, 190, 100
Knapp, G. R., Leggett, S. K., Fan, X., et al. 2004, AJ, 127, 3553
Kratter, K. & Lodato, G. 2016, ARA&A, 54, 271
Kratter, K. M., Murray-Clay, R. A., & Youdin, A. N. 2010, ApJ, 710, 1375
Kroupa, P. 2001, MNRAS, 322, 231
Lagrange, A. M., Bonnefoy, M., Chauvin, G., et al. 2010, Science, 329, 57
Lallement, R., Babusiaux, C., Vergely, J. L., et al. 2019, A&A, 625, A135
Lambrechts, M. & Johansen, A. 2012, A&A, 544, A32
Looper, D. L., Bochanski, J. J., Burgasser, A. J., et al. 2010, AJ, 140, 1486
Looper, D. L., Burgasser, A. J., Kirkpatrick, J. D., & Swift, B. J. 2007, ApJ, 669, L97
Macintosh, B., Graham, J. R., Barman, T., et al. 2015, Science, 350, 64
Macintosh, B., Graham, J. R., Ingraham, P., et al. 2014, Proceedings of the National Academy of Science, 111, 12661
Maire, A.-L., Langlois, M., Dohlen, K., et al. 2016, in Ground-based and Airborne Instrumentation for Astronomy VI, Vol. 9908, 990834
Mamajek, E. E., Bartlett, J. L., Seifahrt, A., et al. 2013, AJ, 146, 154
Marois, C., Lafrenière, D., Doyon, R., Macintosh, B., & Nadeau, D. 2006, ApJ, 641, 556
Marois, C., Macintosh, B., Barman, T., et al. 2008, Science, 322, 1348
Marois, C., Zuckerman, B., Konopacky, Q. M., Macintosh, B., & Barman, T. 2010, Nature, 468, 1080
Martinez, P., Dorrer, C., Aller Carpentier, E., et al. 2009, A&A, 495, 363
Mawet, D., Milli, J., Wahhaj, Z., et al. 2014, ApJ, 792, 97
McElwain, M. W. & Burgasser, A. J. 2006, AJ, 132, 2074
McLean, I. S., McGovern, M. R., Burgasser, A. J., et al. 2003, ApJ, 596, 561
McLean, I. S., Prato, L., McGovern, M. R., et al. 2007, ApJ, 658, 1217
Mellon, S. N., Mamajek, E. E., Oberst, T. E., & Pecaut, M. J. 2017, ApJ, 844, 66
Mordasini, C., Alibert, Y., & Benz, W. 2009a, A&A, 501, 1139
Mordasini, C., Alibert, Y., Benz, W., & Naef, D. 2009b, A&A, 501, 1161
Mordasini, C., van Boekel, R., Mollière, P., Henning, T., & Benneke, B. 2016, ApJ, 832, 41
Muench, A. A., Lada, C. J., Luhman, K. L., Muzerolle, J., & Young, E. 2007, AJ, 134, 411
Mugrauer, M., Röll, T., Ginski, C., et al. 2012, MNRAS, 424, 1714
Nelder, J. A. & Mead, R. 1965, The computer journal, 7, 308
Nielsen, E. L., De Rosa, R. J., Macintosh, B., et al. 2019, AJ, 158, 13
Öberg, K. I., Murray-Clay, R., & Bergin, E. A. 2011, ApJ, 743, L16
Oliphant, T. E. 2006, A guide to NumPy, Vol. 1 (Trelgol Publishing USA)
Ormel, C. W. & Klahr, H. H. 2010, A&A, 520, A43
Paardekooper, S. J. & Mellema, G. 2004, A&A, 425, L9
Pecaut, M. J. & Mamajek, E. E. 2013, ApJS, 208, 9
Pecaut, M. J. & Mamajek, E. E. 2016, MNRAS, 461, 794
Pedregosa, F., Varoquaux, G., Gramfort, A., et al. 2012, arXiv e-prints, arXiv:1201.0490
Pereira, C. B., Franco, C. S., & de Araújo, F. X. 2003, A&A, 397, 927
Pollack, J. B., Hubickyj, O., Bodenheimer, P., et al. 1996, Icarus, 124, 62

[7] Python Software Foundation, https://www.python.org/

Preibisch, T. & Mamajek, E. 2008, The Nearest OB Association: Scorpius-Centaurus (Sco OB2), Vol. 5 (ASP Monograph Publications), 235
Rafikov, R. R. 2005, ApJ, 621, L69
Rameau, J., Chauvin, G., Lagrange, A. M., et al. 2013, The Astrophysical Journal, 772, L15
Rayner, J. T., Cushing, M. C., & Vacca, W. D. 2009, ApJS, 185, 289
Reid, I. N., Lewitus, E., Burgasser, A. J., & Cruz, K. L. 2006, ApJ, 639, 1114
Schmidt, T. O. B., Neuhäuser, R., Seifahrt, A., et al. 2008, A&A, 491, 311
Schwarz, H., Ginski, C., de Kok, R. J., et al. 2016, A&A, 593, A74
Sheehan, P. 2020, Nature, 586, 205
Sheehan, P. D., Tobin, J. J., Federman, S., Megeath, S. T., & Looney, L. W. 2020, ApJ, 902, 141
Sheppard, S. S. & Cushing, M. C. 2009, AJ, 137, 304
Siegler, N., Close, L. M., Burgasser, A. J., et al. 2007, AJ, 133, 2320
Smith, B. A. & Terrile, R. J. 1984, Science, 226, 1421
Soderblom, D. R., Jones, B. F., Balachand ran, S., et al. 1993, AJ, 106, 1059
Soummer, R. 2005, ApJ, 618, L161
Soummer, R., Pueyo, L., & Larkin, J. 2012, ApJ, 755, L28
Stolker, T., Bonse, M. J., Quanz, S. P., et al. 2019, A&A, 621, A59
Stolker, T., Marleau, G. D., Cugno, G., et al. 2020a, A&A, 644, A13
Stolker, T., Quanz, S. P., Todorov, K. O., et al. 2020b, A&A, 635, A182
Torres, C. A. O., Quast, G. R., da Silva, L., et al. 2006, A&A, 460, 695
Van der Walt, S., Schönberger, J. L., Nunez-Iglesias, J., et al. 2014, PeerJ, 2, e453
van Terwisga, S. E., van Dishoeck, E. F., Ansdell, M., et al. 2018, A&A, 616, A88
Vigan, A., Bonavita, M., Biller, B., et al. 2017, A&A, 603, A3
Vigan, A., Fontanive, C., Meyer, M., et al. 2020, arXiv e-prints, arXiv:2007.06573
Vigan, A., Patience, J., Marois, C., et al. 2012, A&A, 544, A9
Virtanen, P., Gommers, R., Oliphant, T. E., et al. 2020, Nature Methods, 17, 261
Voges, W., Aschenbach, B., Boller, T., et al. 1999, A&A, 349, 389
Wahhaj, Z., Milli, J., Romero, C., et al. 2021, arXiv e-prints, arXiv:2101.08268
Wang, J. J., Ginzburg, S., Ren, B., et al. 2020, AJ, 159, 263
Wang, J. J., Graham, J. R., Dawson, R., et al. 2018, AJ, 156, 192
Wang, J. J., Vigan, A., Lacour, S., et al. 2021, arXiv e-prints, arXiv:2101.04187
Wenger, M., Ochsenbein, F., Egret, D., et al. 2000, A&AS, 143, 9
Wertz, O., Absil, O., Gómez González, C. A., et al. 2017, A&A, 598, A83
Zari, E., Hashemi, H., Brown, A. G. A., Jardine, K., & de Zeeuw, P. T. 2018, A&A, 620, A172
Zhu, Z., Hartmann, L., Nelson, R. P., & Gammie, C. F. 2012, ApJ, 746, 110
Zuckerman, B., Rhee, J. H., Song, I., & Bessell, M. S. 2011, ApJ, 732, 61

Appendix A: Observational conditions and setup

We present the observational setup and the weather conditions for our SPHERE observations in Table A.1.

Appendix B: Reference library

The reference libraries were compiled from the full amount of YSES data that were collected under ESO IDs 099.C-0698(A) (PI: Kenworthy), 0101.C-0153(A) (PI: Kenworthy), 0101.C-0341(A) (PI: Bohn), and 106.20X2.001 (PI: Vogt). We used RDI in the innermost region of the images < 1″.2, where the stellar halo was dominating the received flux. We deselected all targets with obvious point sources or extended structures in this region because these signals are not part of the stellar PSF and would therefore deteriorate the quality of our model created by PCA. The remaining targets, their observation epochs, and observing conditions that were used as a reference library for the H and K_s band data are listed in Tables B.1 and B.2, respectively. In the H band we have 269 individual reference frames and in the K_s band we have 164.

Appendix C: Extraction of companion astrometry and photometry

We extracted the companion astrometry and photometry with the `SimplexMinimizationModule` of `PynPoint`. This injects an artificial planet into the data prior to the stellar PSF subtraction with RDI plus PCA. The planet template PSF is obtained from the unsaturated, non-coronagraphic flux images that were taken alongside the observations. The methods injects the artificial planet into the data at the approximate position and magnitude of the real point source, considering the parallactic rotation during the observing sequence. The PSF subtraction is performed using the same library as before (see Appendix B), we smooth the image with a Gaussian kernel with a FWHM of 12 mas (which corresponds to the size of a detector pixel) to reduce pixel-to-pixel variations, and we evaluate the residuals in an aperture with a diameter of ∼ 0″.25 around the injection position. We choose the image curvature, which is represented by the determinant of the Hessian matrix as function of merit, which we aim to minimize by varying the input separation, position angle, and magnitude contrast of our artificial companion. We do not use the absolute value norm as presented by Wertz et al. (2017) as an objective to the minimization because this would not consider large-scale features in the residual image that are not correctly modeled by our PSF subtraction approach. Such a feature is for instance the asymmetric wind driven halo (Cantalloube et al. 2018) that is apparent in the K_s band data in the northeastern to southwestern direction (see right panel of Fig. 2). This uncorrected stellar flux contributes to the planet signal and minimization of the absolute value norm around the planet position would certainly overestimate its flux and perhaps even compromise its astrometry. Planet separation, position angle, and magnitude contrast are optimized simultaneously by a Nelder-Mead simplex minimization algorithm (Nelder & Mead 1965).

Owing to the optimization process our final values for the planetary astrometry and photometry do not exhibit any intrinsic uncertainties. To derive the systematic uncertainties of our injection and minimization approach, we follow the analysis described by Stolker et al. (2020b), using the cube in which the optimized negative planet is injected such that no companion signal remains in the data. For 24 position angles that are equidistantly distributed in polar space we inject positive artificial companions into the data using the same magnitude contrast and the same radial separation as previously determined for our companion. We extract the astrometry and photometry of these artificial companions with the same method as described before and we evaluate the deviations from the injection position and flux. The standard deviation along the 24 distinct positions is utilized as uncertainty of our extraction method. These are combined with additional astrometric uncertainties originating from the detector plate scale, the true north offset, and the centering accuracy of 2.5 mas (see SPHERE manual) to derive the final value of planet separation and position angle as presented in Table 2. For the companion photometry, we add uncertainties due to the variation of the unsaturated stellar PSF throughout the sequence of flux measurements and we account for transmissivity variations of the neutral density filter across the broadband filter that was used for our observations (either the H or K_s band).

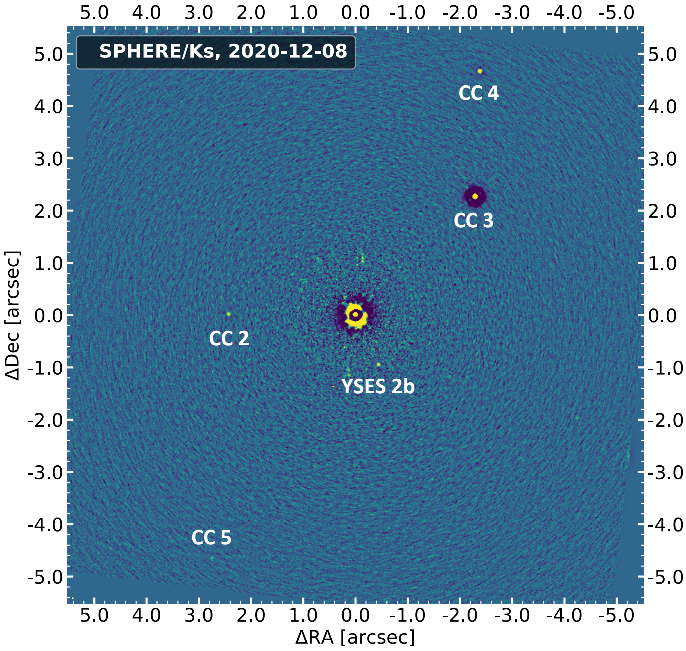


Fig. D.1. Reduced SPHERE data for the full IRDIS field of view. The images are de-rotated and median combined; an unsharp mask is applied to remove the stellar halo. Four additional companion candidates to YSES 2b are identified in the field of view. The image is presented at an arbitrary logarithmic color scale to highlight the off-axis point sources.

Appendix D: Astrometric analysis of background objects

In addition to YSES 2b, there are four candidate companions (CCs) in the SPHERE/IRDIS field of view that we could identify in both observational epochs. These CCs are presented in Fig. D.1, in which we show the de-rotated data from the night of 2020 December 12. No PSF subtraction with RDI is performed, instead we just applied an unsharp mask with a Gaussian kernel size of 5 pixels. YSES 2b can easily be identified in this image product as well. For the remaining CCs, we present the relative astrometric offsets between both observational epochs in the proper motion diagram in Fig. D.2. The relative motions of CCs 2–5 are clearly compatible with stationary background objects, and co-movement can be ruled out for all of them.

Table A.1. SPHERE observations of YSES 2.

Observation date (yyyy-mm-dd)	Filter	FWHM[a] (mas)	NEXP×NDIT×DIT[b] (1×1×s)	$\Delta\pi$[c] (°)	$\langle\omega\rangle$[d] (″)	$\langle X\rangle$[e]	$\langle\tau_0\rangle$[f] (ms)
2018-04-30	H	50.5	4×1×32	0.98	0.87	1.343	6.25
2020-12-08	K_s	61.7	1×18×16	1.37	0.55	1.52	4.30

Notes. [a] Full width at half maximum measured for the non-coronagraphic stellar PSF. [b] NEXP describes the number of exposures, NDIT is the number of subintegrations per exposure, and DIT is the detector integration time of an individual subintegration. [c] $\Delta\pi$ describes the amount of field rotation during the observation, if it is carried out in pupil-stabilized mode (only valid for CI observations). [d] $\langle X\rangle$ denotes the average airmass during the observation. [e] $\langle\omega\rangle$ denotes the average seeing conditions during the observation. [f] $\langle\tau_0\rangle$ denotes the average coherence time during the observation.

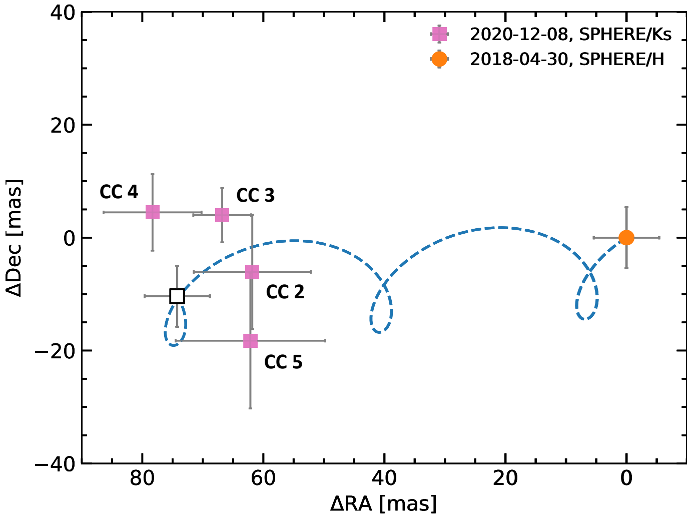


Fig. D.2. Proper motion plot for background objects in the SPHERE/IRDIS field of view. The pink markers indicate the relative astrometric offsets to the first observational epoch that is plotted at the origin of the coordinate system (orange marker). The blue trajectory represents the simulated motion of a static background object at infinity and the white marker shows the relative positional offset of such an object at the time of our second observation.

Table B.1. Reference library for the data reduction in H band.

Target (2MASS ID)	Observation date (yyyy-mm-dd)	NEXP×NDIT×DIT[a] (1×1×s)	$\langle\omega\rangle^{b}$ ($''$)	$\langle X\rangle^{c}$	$\langle\tau_0\rangle^{d}$ (ms)
J11272881-3952572	2017-04-18	4×1×32	1.51	1.10	1.40
J11320835-5803199	2017-06-17	4×1×32	0.67	1.47	2.90
J11445217-6438548	2018-05-14	4×1×32	0.72	1.31	2.38
J11454278-5739285	2018-06-04	4×1×32	0.70	1.19	2.80
J11454278-5739285	2019-01-13	4×1×32	1.14	1.62	3.83
J12065276-5044463	2017-04-02	3×1×32	1.24	1.11	1.50
J12090225-5120410	2018-05-15	4×1×32	0.86	1.12	2.70
J12090225-5120410	2019-12-14	12×2×32	0.63	1.51	7.75
J12101065-4855476	2017-04-18	4×1×32	1.71	1.15	1.40
J12113142-5816533	2018-12-22	3×2×32	1.46	1.47	2.13
J12113142-5816533	2019-02-18	4×2×32	0.45	1.23	14.30
J12160114-5614068	2018-12-27	4×2×32	0.41	1.45	11.88
J12164023-7007361	2018-12-23	3×1×32	0.98	1.59	2.93
J12164023-7007361	2019-02-15	4×1×32	0.54	1.63	11.20
J12185802-5737191	2017-06-17	2×1×32	0.72	1.22	2.70
J12195938-5018404	2018-12-30	4×1×32	0.53	1.62	8.00
J12210499-7116493	2019-01-12	4×2×32	0.80	1.53	4.25
J12220430-4841248	2017-04-18	3×1×32	1.82	1.17	1.40
J12234012-5616325	2017-06-17	4×1×32	0.62	1.72	3.45
J12264842-5215070	2018-12-30	4×1×32	0.40	1.38	8.20
J12302957-5222269	2018-12-30	4×1×32	0.38	1.33	9.85
J12333381-5714066	2019-01-01	4×1×32	0.76	1.37	7.03
J12333381-5714066	2019-01-14	4×1×32	1.26	1.21	2.45
J12361767-5042421	2018-12-30	4×1×32	0.51	1.59	4.68
J12361767-5042421	2019-12-18	16×2×32	1.14	1.57	3.07
J12374883-5209463	2018-12-30	4×1×32	0.41	1.50	7.30
J12383556-5916438	2019-01-03	4×1×32	0.52	1.59	13.90
J12383556-5916438	2019-01-12	4×1×32	0.79	1.26	4.25
J12393796-5731406	2017-06-17	4×1×32	0.64	1.77	3.83
J12404664-5211046	2018-04-30	4×1×32	0.74	1.13	7.05
J12442412-5855216	2017-06-17	4×3×32	0.71	1.37	2.67
J12454884-5410583	2018-04-30	4×1×32	0.71	1.15	6.92
J12480778-4439167	2017-06-17	4×2×32	0.90	1.34	2.75
J12505143-5156353	2019-01-12	4×1×32	1.14	1.32	3.75
J12510556-5253121	2019-01-08	4×1×32	0.58	1.68	3.90
J13015069-5304581	2019-01-08	4×1×32	0.55	1.60	3.95
J13055087-5304181	2018-06-11	4×1×32	0.82	1.14	1.95
J13055087-5304181	2018-07-04	4×1×32	1.73	1.14	1.70
J13064012-5159386	2018-04-30	4×1×32	0.56	1.13	8.15
J13065439-4541313	2018-04-08	4×1×32	0.46	1.09	5.65
J13095880-4527388	2018-05-01	4×1×32	1.08	1.07	2.70
J13103245-4817036	2018-05-01	4×1×32	1.03	1.09	3.30
J13121764-5508258	2017-08-31	4×1×32	0.68	2.22	4.42
J13121764-5508258	2018-05-15	4×1×32	0.62	1.16	2.50
J13174687-4456534	2018-05-28	4×1×32	0.70	1.07	4.33
J13334410-6359345	2017-07-05	4×1×32	1.06	1.53	3.05
J13343188-4209305	2017-04-02	4×1×32	1.14	1.21	1.70
J13354082-4818124	2017-04-02	4×1×32	1.06	1.30	2.08
J13380596-4344564	2017-04-02	4×1×32	1.05	1.32	2.40
J13455599-5222255	2018-04-28	4×1×32	0.64	1.13	6.35

Notes. [(a)] NEXP describes the number of exposures, NDIT is the number of subintegrations per exposure, and DIT is the detector integration time of an individual subintegration. [(b)] $\langle X\rangle$ denotes the average airmass during the observation. [(c)] $\langle\omega\rangle$ denotes the average seeing conditions during the observation. [(d)] $\langle\tau_0\rangle$ denotes the average coherence time during the observation.

Table B.2. Reference library for the data reduction in K_s band.

Target (2MASS ID)	Observation date (yyyy-mm-dd)	NEXP×NDIT×DIT^a (1×1×s)	$\langle\omega\rangle^b$ ($''$)	$\langle X\rangle^c$	$\langle\tau_0\rangle^d$ (ms)
J11445217-6438548	2018-05-14	4×1×32	0.77	1.31	2.60
J11454278-5739285	2019-01-13	4×1×32	1.18	1.59	3.58
J12090225-5120410	2018-05-15	4×1×32	0.70	1.12	2.90
J12113142-5816533	2018-12-22	4×2×32	1.38	1.44	2.05
J12113142-5816533	2019-02-18	4×2×32	0.45	1.22	15.00
J12160114-5614068	2018-12-27	4×2×32	0.47	1.42	10.27
J12164023-7007361	2018-12-23	4×1×32	1.06	1.58	3.43
J12164023-7007361	2019-02-15	4×1×32	0.57	1.61	10.75
J12195938-5018404	2018-12-30	4×1×32	0.55	1.59	9.00
J12210499-7116493	2019-01-12	4×2×32	0.82	1.52	4.40
J12264842-5215070	2018-12-30	4×1×32	0.41	1.36	9.20
J12302957-5222269	2018-12-30	4×1×32	0.45	1.32	7.48
J12333381-5714066	2019-01-01	4×1×32	0.80	1.36	6.25
J12333381-5714066	2019-01-14	4×1×32	1.24	1.21	2.30
J12333381-5714066	2020-12-10	1×20×16	0.58	1.76	5.50
J12361767-5042421	2018-12-30	4×1×32	0.47	1.56	6.22
J12374883-5209463	2018-12-30	4×1×32	0.46	1.48	6.95
J12383556-5916438	2019-01-03	4×1×32	0.46	1.56	12.47
J12383556-5916438	2019-01-12	4×1×32	0.94	1.26	3.45
J12404664-5211046	2018-04-30	4×1×32	0.87	1.13	7.10
J12454884-5410583	2018-04-30	4×1×32	0.66	1.15	8.97
J12505143-5156353	2019-01-12	4×1×32	1.03	1.31	4.10
J12510556-5253121	2019-01-08	4×1×32	0.52	1.65	3.98
J13015069-5304581	2019-01-08	4×1×32	0.49	1.58	4.80
J13055087-5304181	2018-06-11	4×1×32	0.93	1.14	2.02
J13055087-5304181	2018-07-04	4×1×32	1.73	1.14	1.70
J13064012-5159386	2018-04-30	4×1×32	0.56	1.13	9.88
J13065439-4541313	2018-04-08	4×1×32	0.55	1.09	4.68
J13095880-4527388	2018-05-01	4×1×32	1.03	1.07	2.45
J13103245-4817036	2018-05-01	4×1×32	0.87	1.10	4.40
J13121764-5508258	2018-05-15	4×1×32	0.62	1.16	3.00
J13174687-4456534	2018-05-28	4×1×32	0.67	1.07	4.15
J13455599-5222255	2018-04-28	4×1×32	0.65	1.13	6.03

Notes. $^{(a)}$ NEXP describes the number of exposures, NDIT is the number of subintegrations per exposure, and DIT is the detector integration time of an individual subintegration. $^{(b)}$ $\langle X\rangle$ denotes the average airmass during the observation. $^{(c)}$ $\langle\omega\rangle$ denotes the average seeing conditions during the observation. $^{(d)}$ $\langle\tau_0\rangle$ denotes the average coherence time during the observation.